


8-1-2016

## Structural Behavior of NbSexTe2-x Superconductors Under High Pressure

Vahe Mkrtchyan

University of Nevada, Las Vegas, mkrty3@unlv.nevada.edu

Follow this and additional works at: <https://digitalscholarship.unlv.edu/thesesdissertations>

 Part of the [Physical Chemistry Commons](#), [Physics Commons](#), and the [Science and Mathematics Education Commons](#)

---

### Repository Citation

Mkrtchyan, Vahe, "Structural Behavior of NbSexTe2-x Superconductors Under High Pressure" (2016). *UNLV Theses, Dissertations, Professional Papers, and Capstones*. 2796.  
<https://digitalscholarship.unlv.edu/thesesdissertations/2796>

This Thesis is protected by copyright and/or related rights. It has been brought to you by Digital Scholarship@UNLV with permission from the rights-holder(s). You are free to use this Thesis in any way that is permitted by the copyright and related rights legislation that applies to your use. For other uses you need to obtain permission from the rights-holder(s) directly, unless additional rights are indicated by a Creative Commons license in the record and/or on the work itself.

This Thesis has been accepted for inclusion in UNLV Theses, Dissertations, Professional Papers, and Capstones by an authorized administrator of Digital Scholarship@UNLV. For more information, please contact [digitalscholarship@unlv.edu](mailto:digitalscholarship@unlv.edu).

STRUCTURAL BEHAVIOR OF  $\text{NbSe}_x\text{Te}_{2-x}$  SUPERCONDUCTORS UNDER HIGH  
PRESSURE

By

Vahe Mkrtchyan

Bachelor of Science in Physics  
University of Nevada, Las Vegas  
2014

A thesis submitted in partial fulfillment  
of the requirements for the

Master of Science - Physics

Department of Physics and Astronomy  
College of Sciences  
The Graduate College

University of Nevada, Las Vegas  
August 2016



## Thesis Approval

The Graduate College  
The University of Nevada, Las Vegas

July 8, 2016

This thesis prepared by

Vahe Mkrtchyan

entitled

Structural Behavior of  $\text{NbSe}_x\text{Te}_{2-x}$  Superconductors under High Pressure

is approved in partial fulfillment of the requirements for the degree of

Master of Science - Physics  
Department of Physics and Astronomy

Andrew Cornelius, Ph.D.  
*Examination Committee Chair*

Kathryn Hausbeck Korgan, Ph.D.  
*Graduate College Interim Dean*

Ravhi Kumar, Ph.D.  
*Examination Committee Member*

Michael Pravica, Ph.D.  
*Examination Committee Member*

Thomas Hartmann, Ph.D.  
*Graduate College Faculty Representative*

## **Abstract**

### STRUCTURAL BEHAVIOR OF $\text{NbSe}_x\text{Te}_{2-x}$ SUPERCONDUCTORS UNDER HIGH PRESSURE

by

Vahe Mkrtchyan

Dr. Andrew Cornelius, Defense Committee Chair and

Dr. Ravhi Kumar, Defense Committee Co-Chair

University of Nevada, Las Vegas

Niobium chalcogenide compounds have recently gained a great deal of interest due to the fact that a superconducting phase coexists with the charge density wave state (CDW), as well as their potential for numerous applications. Two superconducting compositions,  $\text{NbSe}_x\text{Te}_{2-x}$  ( $x=2, 1.5$ ) were prepared by solid state route using high purity Nb, Se, and Te powders. Powder X-ray diffraction patterns collected at ambient conditions for  $\text{NbSe}_2$  and  $\text{NbSe}_{1.5}\text{Te}_{0.5}$  showed a single phase with hexagonal crystal structure, with space group  $P6_3\text{mmc}$ . High-pressure X-ray diffraction measurements were performed at the Advanced Photon Source at Argonne National Laboratory to investigate structural stability up to 39 GPa. The bulk moduli were found to be 52 GPa for  $\text{NbSe}_2$  and 61.7 GPa for  $\text{NbSe}_{1.5}\text{Te}_{0.5}$  respectively. No pressure induced phase transitions were observed within the studied pressure range.  $T_c$  at ambient pressure was determined to be 7.1 K and 3.35 K for  $\text{NbSe}_2$  and  $\text{NbSe}_{1.5}\text{Te}_{0.5}$  correspondingly. As a superconducting transition was measured under high pressure for  $\text{NbSe}_{1.5}\text{Te}_{0.5}$ . A positive pressure dependence was observed, with the critical temperature increasing from 3.35 K at ambient, to 4.4 K at 1.8 GPa, at a rate of 0.6 K/GPa.

## Acknowledgements

I would like to express my acknowledgements for the assistance of the following people:

Dr. Ravhi Kumar and Dr. Andrew Cornelius for their mentorship, guidance and valuable support throughout the duration of this project.

Dr. Hartmann for the courtesy of allowing us to perform measurements on his PPMS machine.

Jason Baker and Dan Corey for their assistance with the PPMS (Physical Property Measurement System).

Advanced Photon Source at Argonne National Laboratory, and Sector 16 staff in particular with their continuous support during XRD measurements.

Last but not least, I express appreciation to my parents, family members, and friends for their inspirational support.

This research was sponsored by the National Nuclear Security Administration under the Stewardship Science Academic Alliance program through DOE Cooperative Agreement with UNLV.

**Table of Contents**

ABSTRACT..... iii

ACKNOWLEDGEMENTS..... iv

LIST OF TABLES..... vi

LIST OF FIGURES.....vii

CHAPTER 1: INTRODUCTION..... 1

CHAPTER 2: BACKGROUND..... 5

CHAPETER 3: THEORY..... 7

CHAPTER 4: EXPREIMENTAL DETAILS..... 18

CHAPTER 5: RESULTS AND DISCUSSION..... 26

CHAPTER 6: CONCLUSION..... 39

REFERENCES..... 40

CURRICULUM VITAE..... 42

## List of Tables

Table 1	Crystal lattice types.....	8
Table 2	Volume of the unit cell at each pressure point for NbSe <sub>2</sub> .....	27
Table 3	Change of the unit cell volume of NbSe <sub>1.5</sub> Te <sub>0.5</sub> with pressure.....	30

## List of Figures

Figure 1	Expulsion of the magnetic field inside a superconductor.....	2
Figure 2	Diagram of magnetic field dependence on temperature.....	3
Figure 3	Diagram for electron-phonon coupling.....	4
Figure 4	Diffraction of x-ray beams in crystals.....	9
Figure 5	Ruby Fluorescence diagram.....	12
Figure 6	Ruby fluorescence spectrum at different pressures.....	13
Figure 7	Illustration of the two probe method.....	15
Figure 8	Diagram of four probe technique.....	16
Figure 9	Diagram of Van der Pauw configurations.....	17
Figure 10	Solid state reaction furnace.....	18
Figure 11	Synthesis chart for NbSe <sub>2</sub> .....	19
Figure 12	Synthesis chart for NbSe <sub>1.5</sub> Te <sub>0.5</sub> .....	19
Figure 13	Diffraction pattern for NbSe <sub>2</sub> .....	20
Figure 14	Diffraction pattern for NbSe <sub>1.5</sub> Te <sub>0.5</sub> .....	21
Figure 15	Magnetic susceptibility vs temperature for NbSe <sub>2</sub> .....	24
Figure 16	Resistivity as a function of temperature for NbSe <sub>1.5</sub> Te <sub>0.5</sub> at 0 GPa.....	25
Figure 17	The evolution of diffraction patterns for NbSe <sub>2</sub> under pressure.....	26
Figure 18	Pressure vs volume plot for NbSe <sub>2</sub> .....	28
Figure 19	High pressure XRD patterns for NbSe <sub>1.5</sub> Te <sub>0.5</sub> .....	29
Figure 20	Unit cell volume as a function of pressure for NbSe <sub>1.5</sub> Te <sub>0.5</sub> .....	31
Figure 21	Normalized lattice parameters vs pressure plot.....	33
Figure 22	Pressure dependence of a/a <sub>0</sub> (squares) and c/c <sub>0</sub> (circles) for NbS <sub>2</sub> .....	34
Figure 23	Resistivity as a function of temperature from up to 1.80 GPa.....	35
Figure 24	Change of the superconducting temperature as a function of pressure.....	37



Figure 25	The pressure dependence of $T_c$ for $\text{NbSe}_2$ .....	37
-----------	--	----

## Chapter 1: Introduction

Superconductivity is a phenomenon which can be described by two properties: the disappearance of resistance below a certain temperature, known as  $T_c$ , as well as the exclusion of magnetic field below a critical value  $H_c$ . It was discovered by Dutch physicist Heike Onnes in 1911, by studying the electrical properties of mercury at cryogenic temperatures. In 1957, nearly half a century later, the first complete microscopic theory of superconductivity was put forth by Bardeen, Cooper and Schrieffer, called the BCS theory. In 1986, a new field in the study of superconductivity emerged with the discovery of high temperature superconductors, which introduced great challenges to the theory of solid state physics. As it stands, high temperature superconductivity is still an unsolved mystery in physics today.

### 1.1 Properties of Superconductors

#### Meissner Effect

The ejection of magnetic flux from a material below the superconducting temperature subject to a magnetic field is called the Meissner effect. A superconductor actively prevents the magnetic field from penetrating inside the material, therefore making it a perfect diamagnet. The applied field magnetizes the specimen in a direction that opposes the external field, giving it negative magnetic susceptibility [1,2].

$$\chi = \frac{M}{H} = -1 \quad 1$$

In this equation,  $M$  is the magnetization of the material,  $H$  represents the strength of the magnetic field, and  $\chi$  is the susceptibility of the sample.

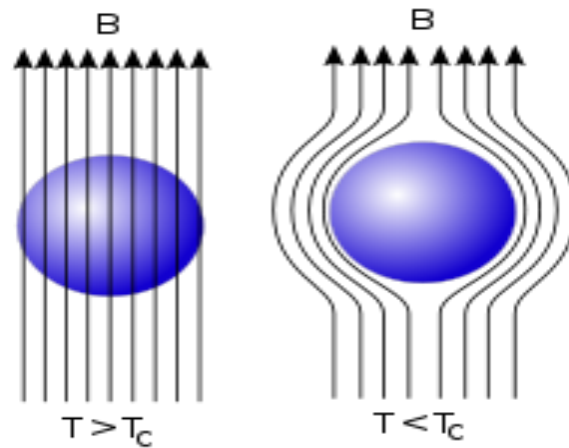


**Figure 1.** Expulsion of the magnetic field inside a superconductor [1].

### Critical Field

The highest value of the magnetic field above which the superconducting state cannot exist is known as critical field,  $H_c$ . Normally, The Meissner effect is observed as long as the applied field does not exceed the critical field, in which case resistance in the material is restored. The value of the critical field is greatest at a temperature of 0 K, and reaches 0 as the critical transition temperature  $T_c$  is approached. The interdependence between critical field and critical temperature is given by the following relation,

$$H_c = H_c(0) \left(1 - \left(\frac{T}{T_c}\right)\right) \quad 2$$

Here,  $H_c$  denotes the strength of the critical field at a given temperature  $T$ , and  $H_c(0)$  is the highest critical field at 0 K.

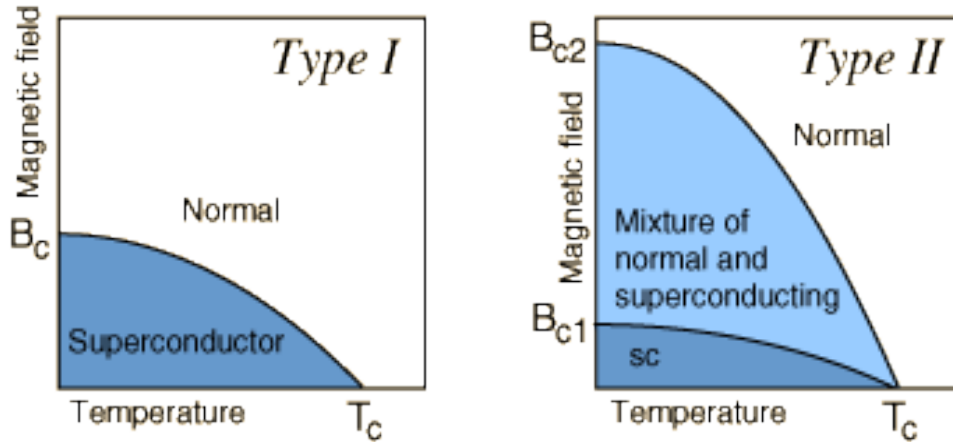


**Figure 2.** Diagram of magnetic field dependence on temperature for type 1 and type 2 superconductors [3].

### Critical Current

The maximum value of electrical current density at which superconductivity is repressed in the material is called the critical current density,  $J_c$  [1]. The critical current density, normally, carries an inversely linear dependence with the critical field, and, usually, decreases upon increasing the external magnetic field. From the point of view of practical applications, the value of the maximum current density that retains superconducting state is the most important parameter when it comes to classifying superconductors [4].

### 1.2 BCS Theory

Since the discovery of superconductivity, many elements and compounds were found to exhibit superconducting properties, but the understanding of the theory behind it was not advanced until 1957, with the introduction of the BCS microscopic quantum mechanical theory, which is now a conventionally accepted basis for describing superconductivity.

The key concept in the BCS theory is the idea of paired electrons close to the Fermi level. The electrons, also known as Cooper pairs, form via phonon coupling. An electron passing

through the lattice feels a momentary attraction from the positive ions, which consequently distorts the lattice. This, in turn, attracts a second electron, thus we interpret it as a coupling of electrons via phonons. The pairing requires two electrons of equal and opposite momentum, and implies a lowering of the electron energy. The pairing model in BCS theory successfully explains the properties demonstrated by the conventional superconductors, and is consistent with experimental observations.

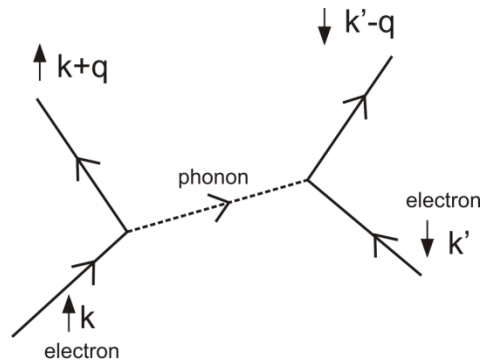


**Figure 3.** Diagram for electron-phonon coupling [3].

## **Chapter 2: Background**

$\text{NbSe}_2$  and  $\text{NbSe}_{1.5}\text{Te}_{0.5}$  are layered transition metal dichalcogenides with a general formula  $\text{MX}_2$ , where M is a transition metal. The interlayer structure of this family of compounds consists of stacked X-M-X layers. The unit cell in the crystal structure has a hexagonal symmetry, and belongs to space group  $\text{P6}_3\text{mmc}$  (194). The two-layered structure  $\text{NbSe}_2$  is a highly anisotropic superconductor, with a critical temperature  $T_c$  of 7.2 K. It, also, undergoes a charge density wave transition around 33 K [5].

As the cuprates, pnictides, and other groups of high temperature superconductors have been slow to emerge in different fields of commercial applications; a lot of focus is shifting back to the research of conventional s-wave superconductors, which are easily fabricated and have higher critical field, and critical current density values, in comparison with the high temperature ceramic superconductors. Layer structured superconductors have acquired great deal of interest since the discovery of superconductivity in  $\text{MgB}_2$ , which is a anisotropic superconductor with two quasi gaps, both having s-symmetry, with an uncharacteristically high transition temperature for a conventional superconductor of 39 K. It was found that the highly anisotropic layer structure of the lattice is responsible for the superconducting behavior in  $\text{MgB}_2$ , which is a type of structure similar to  $\text{NbSe}_2$  and other dichalcogenides [6].

Due to the fact that these compounds are connected with strong in-plane covalent bonds, and much weaker interlayer van-der-Waal forces, the layers are easily cleaved down to a monolayer two-dimensional structure, which exhibit very remarkable properties. A recent paper by Ugeda, *et al.* reported the discovery of superconductivity in single layer  $\text{NbSe}_2$ , which was a breakthrough in the research of 2-D materials. They have discovered that, in contrast with theoretical predictions, charge density wave (CDW) state in  $\text{NbSe}_2$  remained unchanged in the monolayer limit, and exhibited superconductivity at 1.9 K [7]. In the light of this recent discovery, these compounds are promising candidate for applications in nanoscale science.

Our work in high pressure structural and transport studies in  $\text{NbSe}_2$  and  $\text{NbSe}_{1.5}\text{Te}_{0.5}$  was motivated by the recent reports on similar compounds  $\text{FeSe}$ , and  $\text{NbS}_2$ . The work done by Hosono, *et al.* showed that  $\text{FeSe}$  undergoes structural transition from tetragonal to orthorhombic phase around 12 GPa. Their investigation of resistivity under high pressure revealed that  $T_c$  has a linear increase until it reaches the phase boundary, where a kink in the transition temperature is observed, reaching from 8 K at ambient, to a maximum of 34 K at 22 GPa [8]. Also, a paper by Martinez-Pineiro, *et al.* discovered a noticeable effect of applied pressure on the critical temperature of  $\text{FeSe}_{0.5}\text{Te}_{0.5}$ . Similarly, it was shown that  $\text{FeSe}_{1-x}\text{Te}_x$  ( $x = 0.1, 0.2, \text{ and } 0.3$ ) compounds exhibit more rapid increase in  $T_c$  as a function of induced pressure, in comparison with undoped  $\text{FeSe}$ , up to 8 GPa. This observation was explained by a reduction of the Fermi surface nesting, which in turn destabilizes the spin density wave (SDW) state [9], a phenomena that is opposite to what is observed in case with Te doped  $\text{NbSe}_2$  compounds. On the other hand, in a theoretical work done by Liu, *et al.*,  $\text{NbS}_2$  is calculated to maintain the known hexagonal structure up to 26 GPa, after which it transits to a tetragonal phase which remains stable above 200 GPa. More interestingly, it was predicted that  $T_c$  of  $\text{NbS}_2$  should go up with pressure, then jump substantially as the boundary where tetragonal phase develops, and then decrease as the pressure increases [10].

## Chapter 3: Theory

### Crystal Structure

The characteristic and periodic arrangement of atoms and molecules in a solid is known as a crystal. A crystal is described by what is called a unit cell or lattice, which are repeated periodically within the arrangement in three dimensions inside the material. The atoms that lie within the lattice form a basis, which in an ideal case repeat infinitely in certain orientations, depending on the type of the crystal. In mathematical terms, the lattice consists of three translation vectors, which are defined in such a way that if viewed from a given point  $\mathbf{r}$ , the crystal will look identical if translated by an integral multiple of those translation vectors. The above statement can be represented by the following formula:

$$\mathbf{r}' = \mathbf{r} + u_1\mathbf{a} + u_2\mathbf{b} + u_3\mathbf{c} \quad 3$$

Where,  $\mathbf{r}'$  is the point translated with respect to  $\mathbf{r}$ .  $\mathbf{a}$ ,  $\mathbf{b}$ ,  $\mathbf{c}$  are the translation vectors, and  $u_1$ ,  $u_2$ , and  $u_3$  are integer numbers.

Crystals are categorized by the symmetries in the arrangement of points inside the lattice. Such specific symmetries make up 14 different types of lattices, comprising seven types of unit cells. Cubic structure has the greatest level of symmetry, with the sides in all three dimensions being equal and the angles between them forming  $90^\circ$ , whereas triclinic structure is the most asymmetric, with none of the sides or the resulting angles being equal. **Table 1** displays the seven groups of unit cells, along with the corresponding number of lattices matching each group type, as well as the characteristics for the axes and angles for each of them.



Structure Type	Number of Lattices	Unit cell axes and angles
Cubic	3	$a = b = c, \alpha = \beta = \gamma = 90^0$
Tetragonal	2	$a = b \neq c, \alpha = \beta = \gamma = 90^0$
Hexagonal	1	$a = b \neq c, \alpha = \beta = 90^0, \gamma = 120^0$
Trigonal	1	$a = b = c, \alpha = \beta = \gamma < 120^0$
Orthorhombic	4	$a \neq b \neq c, \alpha = \beta = \gamma = 90^0$
Monoclinic	2	$a \neq b \neq c, \alpha = \gamma = 90^0 \neq \beta$
Triclinic	1	$a \neq b \neq c, \alpha \neq \gamma \neq \beta$

**Table 1.** Crystal lattice types [11].

Various physical properties of materials are shaped by this arrangement and periodicity of unit cells, therefore making crystal structure investigations a fundamental necessity to enhance our understanding and to be able to explain the origin of the characteristic properties those materials exhibit [11].

### X-Ray Diffraction

X-ray diffraction (XRD) is a tool used to investigate the crystal structure of materials, by means of identifying the diffraction of electromagnetic waves from lattice planes. X-rays are waves with wavelengths typically ranging from  $0.1 \text{ \AA}$  to  $10 \text{ \AA}$ , with shorter wavelength corresponding to higher energy. They are generated by striking metal anodes with high energy accelerated electrons. X-ray generation is confined inside an x-ray tube, where tungsten filament is heated via application of current and subject to electron ejection and acceleration toward a metal target, which often is made of copper. The collision between incident electrons and

electrons in the copper excite the target electrons to a higher energy state. Upon returning to their ground orbital, the electrons radiate excess energy in the form of X-rays [12].

The x-ray diffraction technique is based upon the periodicity of atomic arrangements inside the unit cell of a crystal. The atomic spacing being in the same range as the radiation wavelength ensures that x-rays get diffracted in the crystal, as shown in **Fig. 4**.

Diffraction can occur only at specific angles for a given spacing between atoms. It is governed by Bragg's Law, given in **Eq. 4**, with strongest diffraction occurring when diffracting beams constructively interfere.

$$2 d \sin\theta = n \lambda \quad 4$$

In this equation,  $\theta$  represents the angle of the incident x-ray beam,  $d$  stands for the spacing between lattice planes, and  $\lambda$  corresponds to the wavelength of the radiation used [12].

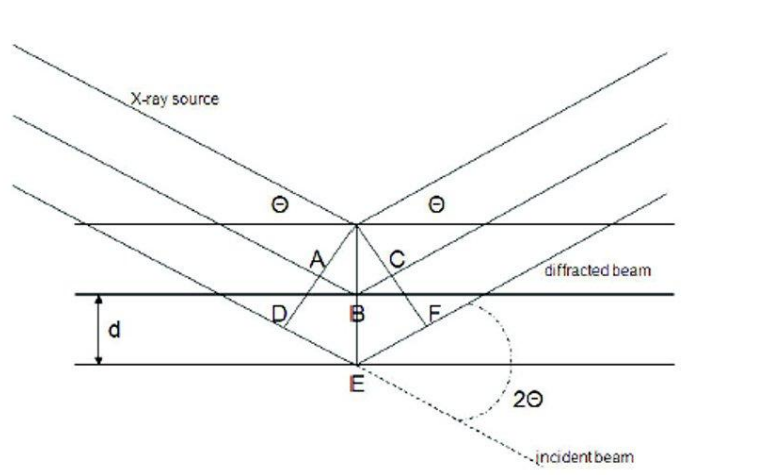


**Figure 4.** Shows the diffraction of x-ray beams in crystals.

XRD techniques are classified into two main categories, single crystal diffraction, and powder diffraction. In the case of single crystal XRD, x-rays of various energies are incident to a single crystalline material which is placed in front of a photographic plate. A characteristic single crystal diffraction pattern consists of multiple diffraction spots surrounding a central point [12].

Patterns obtained from powder diffraction are different, due to the fact that when dealing with powder one has a large number of completely randomly oriented crystals, which diffract from various lattice planes. Bragg's Law must be satisfied to obtain constructive interference from the reflected beam in order to observe diffraction peaks.

Bragg's Law shows that in order to observe diffraction, two parameters can be changed, one can be the energy of the incoming beam (thus the wavelength), and the other parameter is the angle at which the beam impacts at crystal plane. The first case is known as energy-dispersive x-ray diffraction (EDXRD), where the pattern is obtained by scanning the energy of the x-ray while keeping the angle fixed. The second method is called angle-dispersive XRD (ADXRD), when the energy of the incident beam is held fixed, and a range of different angles is scanned. In this project, the angle-dispersive XRD method was used to investigate the crystal structure of our sample compounds.

### Equation of State

Considering an equilibrium state within a system, there are three main properties that characterize the state; pressure, temperature, and volume. Those are called functions of a state. A mathematical formula that combines the interdependence between the state functions is known as an equation of state. The simplest equation of state is one for an ideal gas. Multiple equations of state have been introduced to describe the behavior of more complicated systems such as real gases, fluids, and solids. While, van der Waal's, Redlich-Kwong's, and Virial's equations account for the behavior of gaseous matter, the most commonly used equations in solid state physics are Birch-Murnaghan's, and Vinet's equations of state. Least squares fitting is normally applied to estimate EOS parameters. The choice of the variables that are maintained fixed, and the ones that are refined is important for interpreting the resulting fit values [13]. For our project, Birch-Murnaghan equation of state was preferred in the high pressure analysis,

which is shown in **Eq. 5**.

$$P(V) = \frac{3B_0}{2} \left[ \left( \frac{V_0}{V} \right)^{\frac{7}{3}} - \left( \frac{V_0}{V} \right)^{\frac{5}{3}} \right] \left[ 1 + \frac{3}{4} (B'_0 - 4) \left( \left( \frac{V_0}{V} \right)^{\frac{2}{3}} - 1 \right) \right] \quad 5$$

This equation provides the relation between pressure and cell volume when the temperature is maintained unchanged.  $V_0$  is the initial volume of the unit cell in this relation, where as  $B_0$  is the bulk modulus, and  $B'_0$  being the first pressure derivative of the bulk modulus [14].

### Ruby Fluorescence

There are two conventional techniques for determining the pressure inside a high pressure device, such as DACs (diamond anvil cells). One of those techniques is to determine the pressure by measuring fluorescence line shift from ruby placed inside the pressure chamber. The other method is determining the pressure from x-ray diffraction data of a pressure marker: normally a metal which has a volume dependence as a function of pressure, that has been well studied. The unit cell volume in the later case is determined from the high pressure x-ray pattern. In my project, ruby fluorescence was used for pressure measurement in HPXRD experiments.

Ruby,  $\text{Al}_2\text{O}_3$  doped with  $\text{Cr}^{3+}$ , plays a fundamental role in modern science, being used as a pressure marker in high pressure experiments. The idea that shift of  $R_1$  and  $R_2$  lines of ruby under pressure can be used as a pressure sensor was originally proposed by Formann *et al.*, and has soon become a widely used scientific tool. When ruby is subject to radiation, the ground state electron in  $\text{Cr}^{3+}$  jump into excited states  $E_3$  and  $E_4$ , and shortly after fall into a state  $E_2$ , as illustrated in **Fig. 5**. The transition from excited states to the meta-stable occurs very fast, and is non-radiative. On the other hand, when the electrons eventually decay from the meta-stable state  $E_2$  down to the ground state, radiation is released in the form of photons.

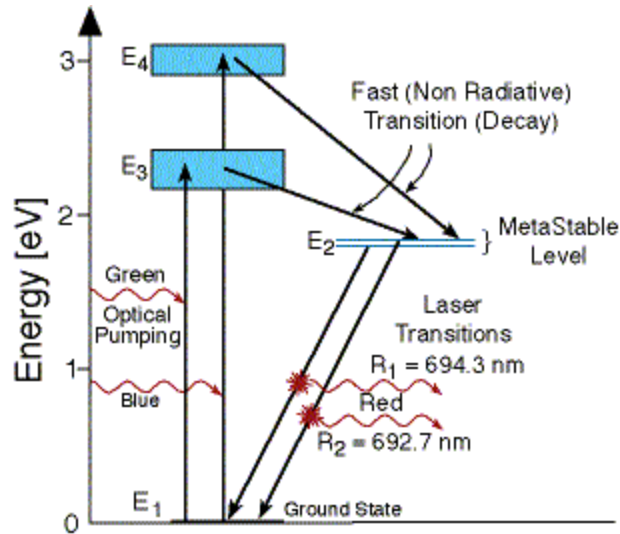


**Figure 5.** Ruby Fluorescence diagram [15].

Since,  $E_2$  state is comprised of two different energy levels due to spin splitting; the photons released during the transition from  $E_2$  to ground state have different energies as well. The photons resulting due to the decay from the higher energy level in  $E_2$  state are known as  $R_1$  ruby line, while the ones released during the transition from the lower level correspond to  $R_2$  line in ruby spectrum.

Upon application of pressure to ruby, the energy difference changes between the ground state and electrons are promoted to excited states, particularly the two states at  $E_2$  level. This change in energy difference has been studied in depth, and as ruby fluoresces, the pressure is determined from the change in the wavelength of the emitted photons.

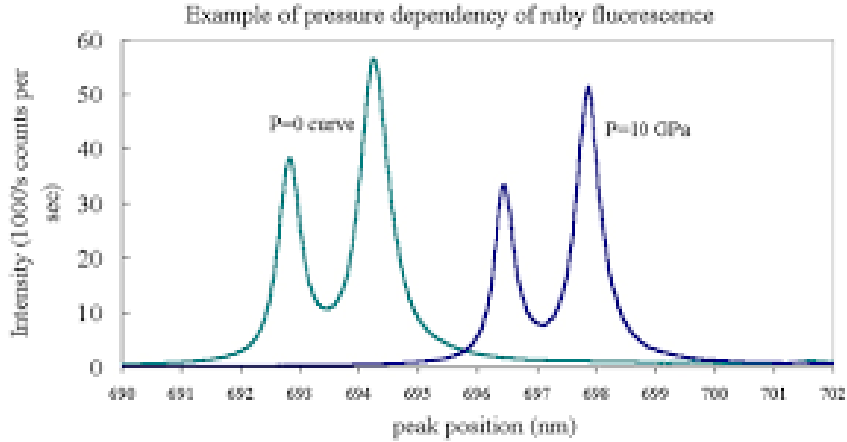


**Figure 6.** Ruby fluorescence spectrum at different pressures [16].

**Fig. 6** shows an illustration of the ruby fluorescence spectrum. The green curve corresponds to the spectrum at ambient pressure, and the purple curve corresponds to the spectrum at 10 GPa. As discussed, the change in pressure affects the wavelength of the emitted light, and this results in shifts of the peak positions. The peak at higher wavelength represents the  $R_1$  line, as it corresponds to the higher energy decay. The peak at lower wavelength is the  $R_2$  line in the ruby fluorescence spectrum.

Ruby pressure scales are calibrated by placing rubies inside a pressure cell along with another pressure marker with a known pressure vs volume dependence. The pressure is estimated from the known marker, and fitted to the corresponding shift in the R line peak in the ruby spectrum. Multiple calibration curves were obtained over the course of time for various pressure ranges, however the most commonly used scale was developed by Mao *et al.*, in 1977. This scale estimates the pressure by accounting for the shift in  $R_1$  line with respect to the ambient wavelength [17]. The pressure curve is fit to the equation

$$P = 380.8 \left[ \left( \frac{\lambda}{694.2} \right)^5 - 1 \right] \quad 6$$

From this equation, it is evident that when the wavelength of the  $R_1$  peak is 694.2 nm, then corresponding pressure is equal to 0 GPa. However, if we apply a pressure of 10 GPa, we would

expect to observe the peak around 698 nm. This pressure scale has been determined to be valid for pressures up to at least 80 GPa, which was suitable for our experiment.

### Resistivity Measurement Methods

Resistivity is a physical property that is specific to each material. It is calculated by measuring resistance from a given size of a sample, given that the dimensions of the sample are known.

$$\rho = \frac{R A}{l} \tag{7}$$

In this equation,  $\rho$  denotes the resistivity,  $R$  is the resistance, and  $l$  and  $A$  correspond to the length

and the cross-sectional area of the sample respectively. There are three general ways to measure resistivity; the two probe method, the four probe method, and the Van der Pauw method.

#### **a) Two probe method**

The two probe method uses only two leads that pass from the resistance measuring device to the sample. In this case, voltage and current are carried from the source by the same pair of leads.

$$V = (I - I_v)(R_{sample} + 2R_{contact} + 2R_{lead}) - 2I_v R_{lead} \tag{8}$$

**Eq. 8** shows the mathematical representation of the two probe method, where  $I$  is the current generated in the current source,  $I_v$  is the current passing through the voltmeter.

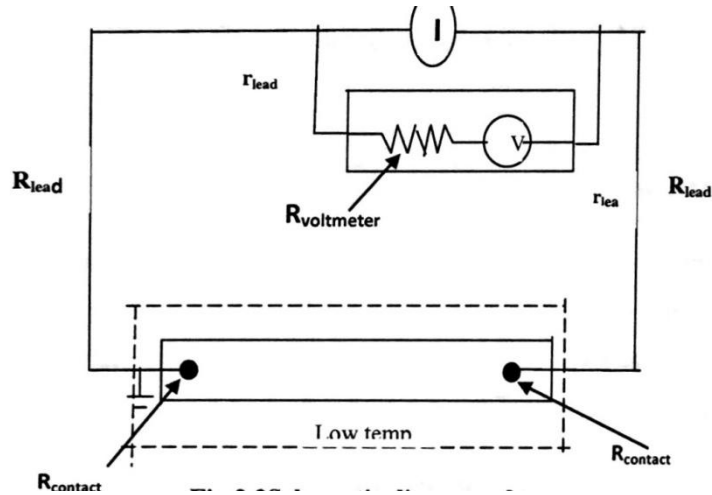


**Figure 7.** Illustration of the two probe method [18]

Given that the internal resistance of the voltmeter normally ranges around 1-10 GΩ, the voltmeter current is much less than the current generated by the source meter, and **Eq. 8** can be reduced to:

$$V = I(R_{sample} + 2R_{contact} + 2R_{lead}) \quad 9$$

The samples suitable for two probe resistivity tests may be in the shape of a bar or a strip.

#### **b) Four Probe Method**

In four probe method, there are four separate leads that connect to the sample, each carrying current or voltage separately. The outer leads are the probes for the current, and the inner leads measure the voltage across the area where the current passes.



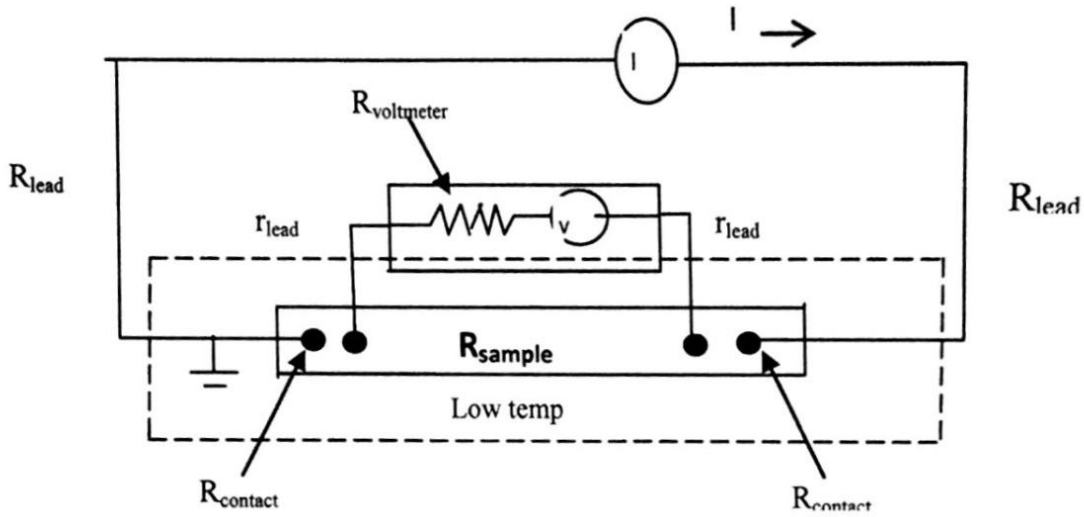


**Figure 8.** Provides a diagram of four probe technique [18].

The formula for determining the voltage with this method is shown in **Eq. 10**.

$$V = (I - I_v)(R_{sample}) - I(2R_{contact} + 2R_{lead}) \quad 10$$

Again, assuming that the internal resistance of the voltmeter is much larger than that of the circuit,

Eq. 10 simply yields to;

$$V = I(R_{sample}) \quad 11$$

The four probe method is more advantageous compared to the two probe method as it provides more accurate reading of the actual sample resistance due to the fact that it eliminates the contributions from other sources, such as the contact resistance and the probe resistance.

### c) Van der Pauw Method

Two and four probe techniques fail to provide sufficiently accurate measurements of the resistivity unless the specimen has a rectangular shape. In the case of irregularly shaped materials, the Van der Pauw method is preferred.

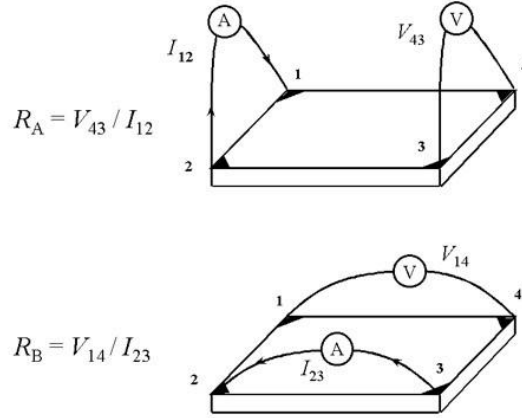


**Figure 9.** Diagram of Van der Pauw configurations [19].

This technique relies on measuring two separate resistance values, shown in **Fig. 9**. The overall sample resistance can be evaluated from these  $R_a$  and  $R_b$  values, using Van der Pauw formula presented in **Eq. 12**.

$$e^{\frac{-\pi R_A}{R_s}} + e^{\frac{-\pi R_B}{R_s}} = 1 \quad 12$$

$R_s$  corresponds to the sample resistance, in the equation above.

In case where the values of  $R_a$  and  $R_b$  are of the same magnitude, the resistivity of the sample can be obtained from Eq. 13. Otherwise, Eq. 14 is used to calculate resistivity if  $R_a$  and  $R_b$  are different.

$$\rho = \frac{\pi d}{\ln 2} \frac{R_A + R_B}{2} \quad 13$$

$$\rho = \frac{\pi d}{\ln 2} \frac{R_A + R_B}{2} f\left(\frac{R_A}{R_B}\right) \quad 14$$

The requirements for proper Van de Pauw measurements are; that the thickness of the sample should be negligible in comparison with the area of the surface, the geometrical shape should be symmetrical, and, the probes placed at the edges of the sample and contacts must be much smaller than the surface area [20].

## **Chapter 4: Experimental Details**

### **Sample Synthesis**

$\text{NbSe}_2$  and  $\text{NbSe}_{1.5}\text{Te}_{0.5}$  were synthesized with starting materials Nb, Se, and Te powders of high purity (99.995%), manufactured by Alpha Aesar and Sigma Aldrich. Constituent elements were carefully weighed and prepared in proper stoichiometric ratios, plus 5% excess selenium, and uniformly mixed using an agate mortar and pestle. The resulting powder was pressed into a pellet inside a 7 mm pellet die was pressurized under 3500 psi. The pellets were then sealed in a quartz tube and placed into a furnace. An MTI 9200 furnace was used for synthesis, which was programmed to heat the samples up to  $750^\circ\text{C}$  at a rate of 10 K/min, and to keep the temperature stable for 16 hours.



**Figure 10.** Solid state reaction furnace.

After the tubes were cooled to ambient temperature, the pellets were then taken out, ground for homogeneity, re-pelletized, resealed in a tube and placed back into the furnace for annealing at  $600^\circ\text{C}$  for 96 hours. Upon completion of the annealing process, the pellets were extracted and, then, broken down into two pieces. One piece was finely ground for XRD experiments, and the other piece was used for electrical transport measurements.

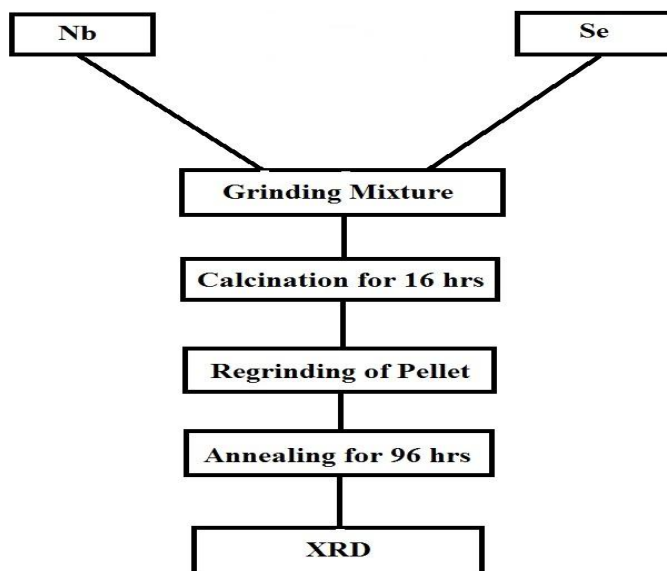


**Figure 11.** Synthesis chart for NbSe<sub>2</sub>

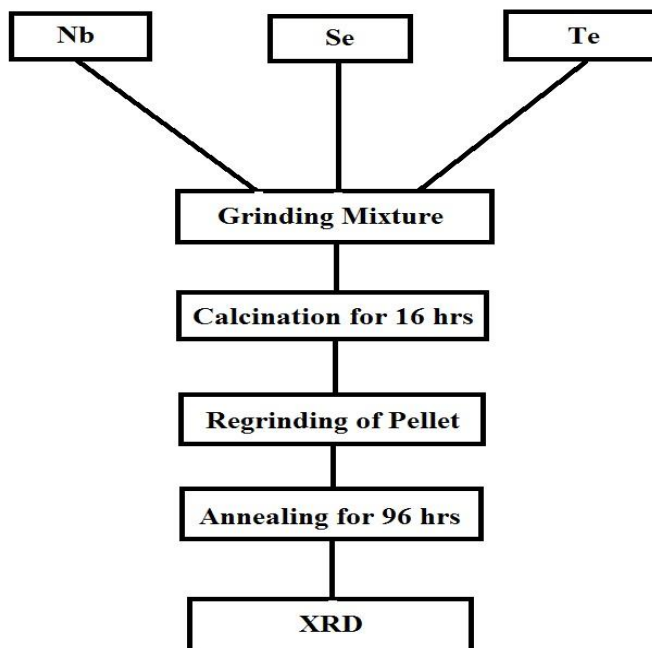


**Figure 12.** Synthesis chart for NbSe<sub>1.5</sub>Te<sub>0.5</sub>

### Ambient Characterization

Phase analysis was conducted using room temperature (RT) powder XRD measurements with an angle dispersive X-ray apparatus with a CuK- $\alpha$  ( $\lambda = 1.5418 \text{ \AA}$ ) source. The measurements were performed in an effort to check phase purity as well as to determine the crystal structure and lattice parameters of the samples. The samples were scanned from  $20^{\circ}$ - $70^{\circ}$  for NbSe<sub>2</sub> sample, and  $20^{\circ}$ - $80^{\circ}$  for NbSe<sub>1.5</sub>Te<sub>0.5</sub>, with a scanning rate of  $1^{\circ}/\text{min}$ . The XRD patterns obtained were compared to the literature, and the results were matched with a pattern for NbSe<sub>2</sub> from the standard ICDD database. Also, a reference pattern was simulated using Powdercell software.

Separate plots for both compounds, NbSe<sub>2</sub> and NbSe<sub>1.5</sub>Te<sub>0.5</sub> are presented in **Fig. 13 and 14** respectively. The well defined peaks in the patterns suggest the presence of a single phase in our specimen. Along with the dominating peaks, a few smaller peaks were observed that do not correspond to NbSe<sub>2</sub> phase, which are assumed to be small fractions of impurity in our samples. In order to determine the lattice parameters, the patterns were indexed using MDI Jade 7.1 software[21]. The data was fitted to P6<sub>3</sub>mmc hexagonal structure, with space group 194.

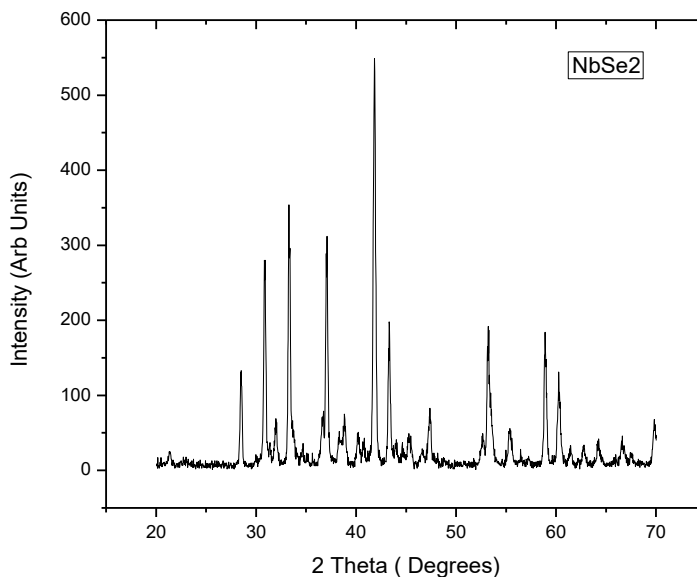


**Figure 13.** Diffraction pattern for NbSe<sub>2</sub>

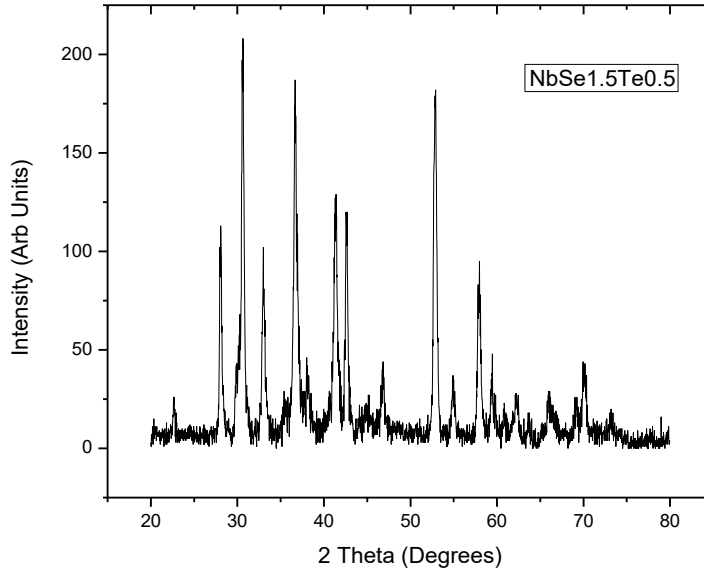


**Figure 14.** Diffraction pattern for NbSe<sub>1.5</sub>Te<sub>0.5</sub>

The unit cell parameter **a** for NbSe<sub>2</sub> was determined to be 3.442 (2) Å, and the value of parameter **c** = 12.539 (2) Å. These values compare well with the numbers found in the literature, which state that niobium diselenide crystallizes with inner atomic spacing of **a** = 3.4425 (5) Å and **c** = 12.547 (3) Å [22]. The unit cell parameters for NbSe<sub>1.5</sub>Te<sub>0.5</sub> were calculated at **a** = 3.461 (2) Å, and **c** = 12.728 (5) Å.

#### HPXRD Measurements

Two sets of high pressure x-ray diffraction measurements were performed on the synthesized compounds at station ID-B of Sector 16 at the Advanced Photon Source at Argonne National Laboratory.

Symmetric panoramic diamond anvil cells (DACs) were used to pressurize the samples. The DAC is comprised of two diamonds that are glued to backing plates made out of beryllium, which are attached to two stainless steel pieces that serve as a frame for the DAC. When the sample is loaded inside the cell, the two pieces are manually brought together and pressure is produced by tightening four screws threaded into the frame. However, before the DAC is closed, the diamonds need to be aligned. Following diamond alignment, the gasket is pre-indented. A gasket made of rhenium was used with a thickness of 250  $\mu\text{m}$ . After initial indentation of the gasket, the thickness of the gasket was reduced to around 50  $\mu\text{m}$  near the area of the diamond culets. Lastly, a hole was drilled in the indented section of the gasket, which served as a sample chamber upon the compression of the DAC. The sample was then loaded in the cell, along with a ruby sphere, which was used as a pressure calibrant. The cell was assembled and tightened in neon gas environment. While, increasing the pressure slightly in the DAC, neon gas was trapped inside the sample chamber and was used as a pressure transmitting medium to ensure that the sample was subjected to hydrostatic pressure throughout the experiment.

The insertion device beam line (16 ID-B) has been calibrated for x-ray energy prior to beginning the experiment with a known sample in order to determine the wavelength of the x-ray radiation, as well as other parameters needed for the analysis of the patterns, such as sample detector distance. The diamond anvil cells (DACs) were subjected to direct beam exposure for 10-20 seconds at each pressure point. Once the beam was diffracted from the sample, the reflected photons were collected on an image plate. The wavelength of the x-ray beam was determined to be 0.406626  $\text{\AA}$ .

The pressure was adjusted either *in-situ*, with a membrane, or by hand tightening. Initial pressure increments for pressures under 15 GPa ranged between 0.5 GPa and 1.5 GPa per step, and 2-4 GPa at pressures above 15 GPa, up to 40 GPa range. The pressure inside the cell was determined using ruby fluorescence method.

Once the data from high pressure XRD experiments was collected, it was then analyzed using FIT2D [23] and MDI Jade software. The raw files containing the data from the CCD detector were integrated with FIT2D, using the calibration parameters obtained earlier. As a result, two dimensional diffraction patterns were produced. MDI Jade was then used to obtain the lattice parameters, as well as the unit cell volume, similar to the case with ambient XRD measurements. Once, the cell volumes were determined, a pressure vs volume curve was constructed, for both samples, to calculate the equation of state. EOS 7.1 software was used to produce the Birch-Murnaghan third order fit lines, accompanied with the corresponding fit parameters.

#### Ambient and High Pressure Transport Measurements

Two sets of ambient and high pressure resistivity measurements were performed on both compounds in order to investigate the superconducting behavior. A physical properties measurement system (PPMS) from Quantum Design was used to conduct low temperature experiments. The system, cooled by liquid helium, allows reaching temperatures as low as 2 K inside the cryo chamber.

Ambient magnetic susceptibility measurements were performed on NbSe<sub>2</sub>. Susceptibility vs temperature data was collected at 3 oscillating fields of 0.1, 1, and 10 Oe, shown in **Fig. 15**. The transition temperature for NbSe<sub>2</sub> was determined to be 7.1 K, which is consistent with literature values.



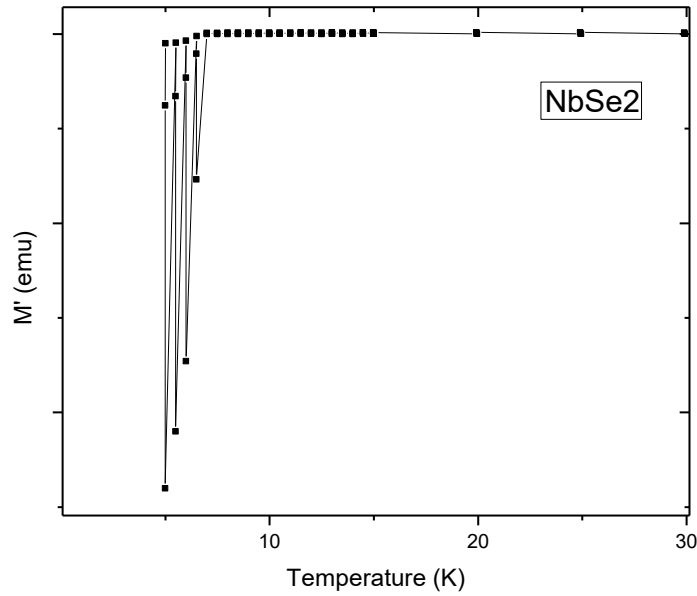


**Figure 15.** Magnetic susceptibility vs temperature for NbSe<sub>2</sub>

Resistivity measurements were performed on NbSe<sub>1.5</sub>Te<sub>0.5</sub> using Quantum Design resistivity puck. A piece of NbSe<sub>1.5</sub>Te<sub>0.5</sub> was cut in a bar shape and placed on the surface of the puck, with a thin layer of low temperature grease between the puck and the sample in order to ensure proper thermal contact. Conventional four probe technique was applied to measure resistivity. Silver paste epoxy was used to secure the current and voltage leads on the sample. The results obtained from ambient measurements, as illustrated in **Fig. 16**, confirmed the existence of the superconducting state in the compound under temperature  $T_c$  of 3.35 K.

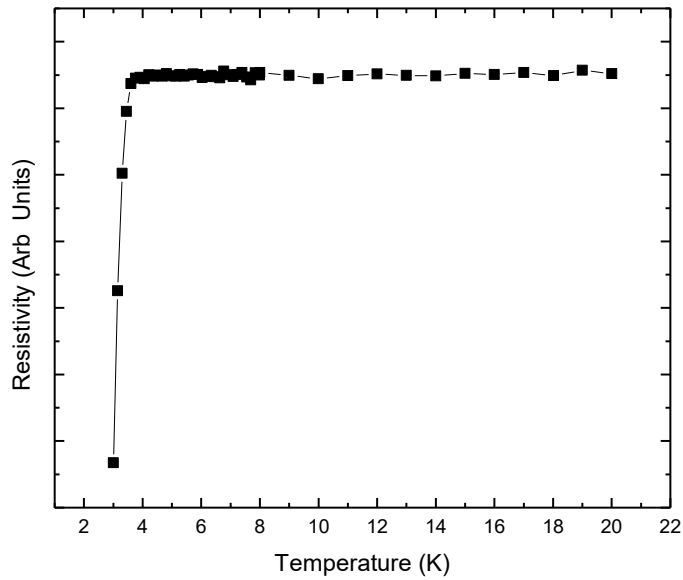


**Figure 16.** Resistivity as a function of temperature for NbSe<sub>1.5</sub>Te<sub>0.5</sub> at 0 GPa

High pressure resistivity data was collected using an Easy Lab piston type pressure cell. Pressures upwards of 3 GPa can be achieved with this cell. The sample was placed inside a cylindrical teflon tube, which served as a sample chamber, along with tin wire for pressure calculation. The pressure dependence of the transition temperature  $T_c$  for Sn has been well studied, and allowed us to estimate the pressure inside the cell at low temperature. The tube was, then, filled with Daphne oil as a pressure transmitting medium, and closed with a metal piston on one side, and a supporting feed through on the other side. A set of four copper wires extended out of the feed through and were soldered onto a regular PPMS puck for resistivity measurements. The pressure was generated by pushing the piston inwards with the use of a hydraulic press, and locking the upper nut in position.

## Chapter 5: Results and Discussion

### NbSe<sub>2</sub> HPXRD

High pressure x-ray diffraction data were collected up to 39 GPa for the NbSe<sub>2</sub>. Using the Fit2D program described earlier, the high pressure x-ray patterns were integrated and the results are presented in **Fig. 17**. Aside from the normal shift to higher angles with pressure, no new peaks are observed in the high pressure regions, nor any peak splitting, therefore the patterns show no evidence of any phase transitions within the studied pressure range. The data was successfully indexed to hexagonal crystal structure (Space group *P6<sub>3</sub>mmc*).

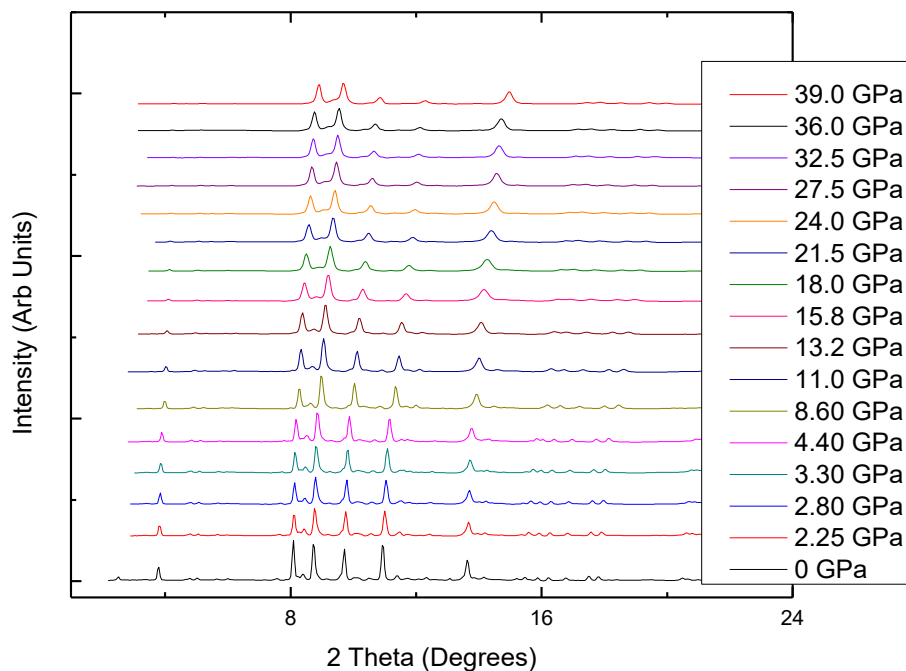


**Figure 17.** Evolution of diffraction patterns for NbSe<sub>2</sub> under pressure.

The unit cell parameters were obtained with MDI Jade software. The peak positions at each pressure point were indexed to the given structure to obtain the dimensions of the hexagonal prisms in **a** and **b** directions, as well as the height of the unit cell in **c** direction. With the lattice constants determined, the unit cell volume was then calculated, and is shown in **Table 4**. The errors of the unit cell volume values were estimated by propagating the errors on the lattice parameters from Jade.

Pressure (GPa)	Volume ( $\text{\AA}^3$ )	Error ( $\text{\AA}^3$ )
0	128.9	0.19
2.25	123.76	0.21
2.8	122.83	0.17
3.3	120.85	0.24
4.4	119.34	0.22
6.5	115.72	0.27
8.6	113.48	0.19
11	110.75	0.25
13.2	108.88	0.29
15.8	104.99	0.24
18	102.76	0.32
21.5	99.74	0.26
24	98.13	0.14
27.5	96.29	0.21
32.5	93.78	0.2
36	91.43	0.27
39	89.91	0.24

**Table 2.** Presents the volume of the unit cell at each pressure point for NbSe<sub>2</sub>

The results obtained were used for equation of state analysis. The change in the volume of the unit cell as a function of pressure is displayed in **Fig. 18**. 3<sup>rd</sup> order Birch-Murnaghan EOS was fit to the plot. The value for the bulk modulus for NbSe<sub>2</sub> up to 39 GPa was determined to be 52.0 (7.4) GPa, which agrees well with the results obtained by Ehm, *et al.* for a similar compound NbS<sub>2</sub>, where the **B**<sub>0</sub> was calculated to be 57 (1) GPa. The other fitted parameter, the initial volume **V**<sub>0</sub> was estimated to be 128.5 (1.5) Å<sup>3</sup>, which agrees very well with the experimentally obtained value of 128.65 (0.20) Å<sup>3</sup> from ambient x-ray diffraction measurement. The pressure derivative of bulk modulus **B**<sub>0</sub> was 4.1 (0.3).

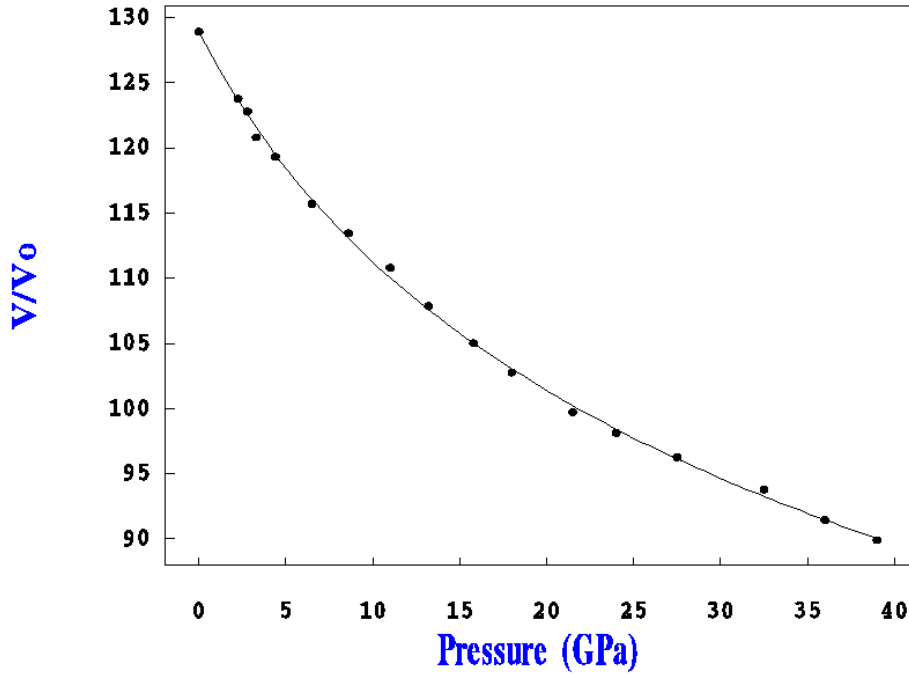


**Figure 18.** Pressure vs volume plot for NbSe<sub>2</sub> fitted with 3<sup>rd</sup> order Birch-Murnaghan EOS

### NbSe<sub>1.5</sub>Te<sub>0.5</sub> HPXRD Results

Similar high pressure x-ray diffraction analysis was done for the Te doped sample. As in the case with NbSe<sub>2</sub>, the patterns obtained from NbSe<sub>1.5</sub>Te<sub>0.5</sub> at high pressure regions revealed the absence of peak splitting, indicating the stability of the ambient hexagonal *P63mmc* phase up to at least 39.1 GPa. **Fig. 19** shows how XRD patterns evolve upon increasing the pressure. As observed from the plot, the intensities of the peaks change for NbSe<sub>1.5</sub>Te<sub>0.5</sub> at various pressures. This phenomenon can be attributed to a change of the positions of the Se atoms with the introduction of a small Te concentration to the interlayer prisms. The atomic position of Nb remain unchanged within the unit cell with increasing pressure, along with the a and b parameters of the Se atoms, However, the z parameter of the position of selenium atoms does change slightly, which may account for the variation of the peak intensities.

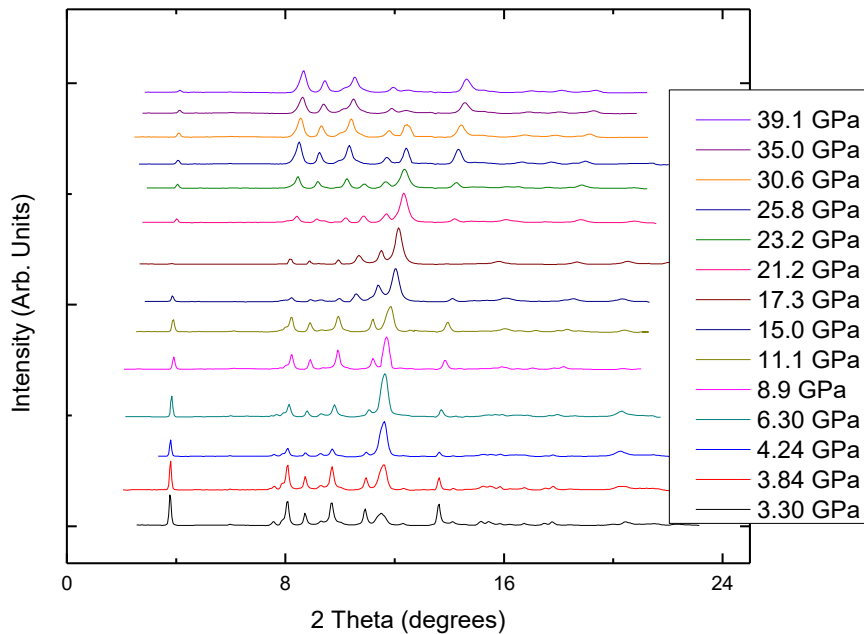


**Figure 19.** High pressure XRD patterns for NbSe<sub>1.5</sub>Te<sub>0.5</sub>

The lattice parameters **a** and **c** were determined from the diffraction patterns using Jade. The dimensions of the unit cell, were found to be slightly larger than of the NbSe<sub>2</sub> sample. **Table 3** presents the values for the unit cell volume at different pressures, as calculated by indexing the patterns to the characteristic space group.

Pressure (GPa)	Volume (Å <sup>3</sup> )	Error (Å <sup>3</sup> )
0	132.47	0.22
3.3	125.57	0.24
3.84	124.94	0.19
6.3	121.73	0.21
8.9	118.28	0.24
11.1	116.4	0.18
15	113.03	0.28
17.3	109.16	0.24
21.2	107.36	0.2
23.2	106.03	0.19
25.8	103.92	0.23
30.6	101.55	0.32
35	99.28	0.27
39.1	97.89	0.23

**Table 3.** Change of the unit cell volume of NbSe<sub>1.5</sub>Te<sub>0.5</sub> with pressure.

3<sup>rd</sup> order Birch-Murnaghan EOS fit was obtained after plotting pressure as a function of unit cell volume. The values for the bulk modulus and the cell volume were determined as  $B_0 = 61.7 (10)$  GPa,  $V_0 = 132.6 (1.3) \text{ \AA}^3$ , and  $B'_0 = 4.56 (0.7)$ . The value for the initial cell volume obtained from the fit is in very good agreement with the results from ambient pressure x-ray diffraction measurements of  $V_0 = 132.05 (0.3) \text{ \AA}^3$ . The calculated value for the bulk modulus for  $\text{NbSe}_{1.5}\text{Te}_{0.5}$  is found to be larger than of  $\text{NbSe}_2$  sample,  $B_0 = 52 (7.4)$  GPa, and  $\text{NbS}_2$  determined by *Ehm et al.* ( $B_0 = 57$  GPa) [24]. However, the increase in bulk modulus agrees well with the results published by *Ciechan et al.* for similar compounds  $\text{FeSe}$  and  $\text{FeSe}_{0.5}\text{Te}_{0.5}$ , where it was determined that the sample having Se partially substituted with Te had a larger bulk modulus than the undoped sample.

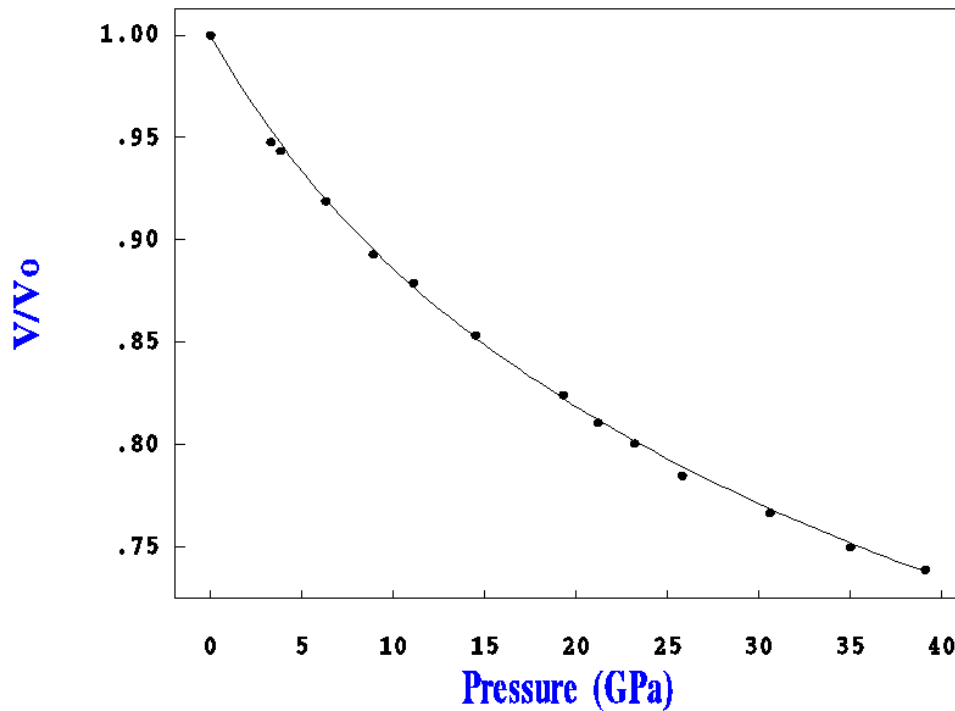


**Figure 20.** Change of unit cell volume as a function of pressure for  $\text{NbSe}_{1.5}\text{Te}_{0.5}$



### Compressibility of NbSe<sub>2</sub> and NbSe<sub>1.5</sub>Te<sub>0.5</sub>

The effect of pressure on the compressibility of lattice has also been investigated. **Fig. 21** depicts the pressure dependence of **a** and **c** axes separately, where the changes of the normalized and the  $\mathbf{a}/\mathbf{a}_0$  and  $\mathbf{c}/\mathbf{c}_0$  lattice constants have been plotted as functions of pressure for NbSe<sub>2</sub> and NbSe<sub>1.5</sub>Te<sub>0.5</sub>. The results show highly anisotropic behavior in compressibility. The compression along the **c** axis is almost twice as large as the compression along the **a** and **b** axes for both compounds. Lattice parameters **a** and **c** up to 3.3 GPa were used to fit a function in order to determine the linear compressibility factor **k**. The magnitude of anisotropy is found to be in the same order of magnitude when compared to similar dichalcogenides. The values for linear compressibility along the **a** and **b** axis were calculated to be  $\mathbf{k}_a = 0.0033$  (2) GPa<sup>-1</sup> for NbSe<sub>2</sub>, and  $\mathbf{k}_a = 0.0029$  (3) GPa<sup>-1</sup> for NbSe<sub>1.5</sub>Te<sub>0.5</sub>. Similarly, the compressibility factors along direction **c** are;  $\mathbf{k}_c = 0.0174$  (3) GPa<sup>-1</sup> and  $\mathbf{k}_c = 0.0115$  (5) GPa<sup>-1</sup> for NbSe<sub>2</sub> and NbSe<sub>1.5</sub>Te<sub>0.5</sub> correspondingly. This data is in good agreement with other results found in the literature for NbSe<sub>2</sub>, obtained by Jones *et al.* [25], where the linear compressibility was derived in a pressure range up to 4.8 GPa of  $\mathbf{k}_a = 0.0041$  (4) GPa<sup>-1</sup> and  $\mathbf{k}_c = 0.0162$  (5) GPa<sup>-1</sup>. Our experimental results, also, match well with values found in the paper by Ehm *et al.* for NbS<sub>2</sub> transition metal dichalcogenide **Fig. 22**. According to them, the anisotropy ratio in compressibility between **c** and **a** axis was determined to be 2.5, also, the compression factor **k** was 0.0039 (3) GPa<sup>-1</sup> parallel to **a** axis, and 0.010 (4) GPa<sup>-1</sup> along **c** direction.

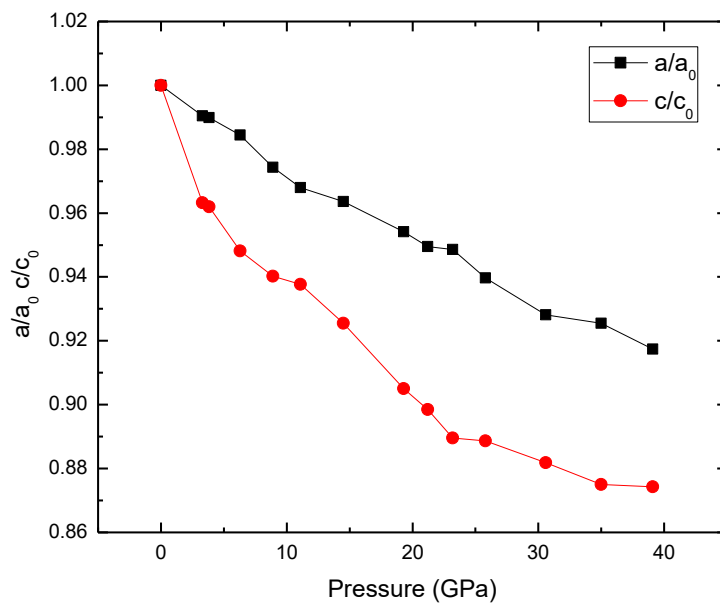
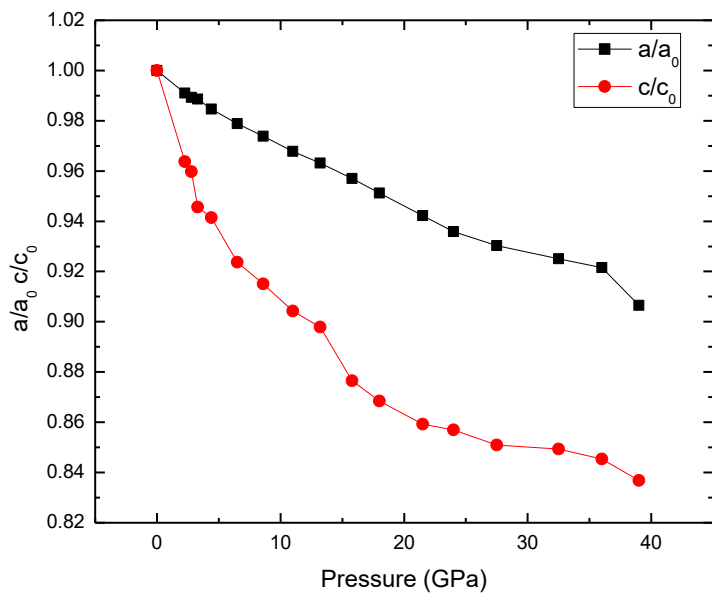


**Figure 21.** Evolution of the normalized lattice parameters for NbSe<sub>2</sub> (top) and NbSe<sub>1.5</sub>Te<sub>0.5</sub> (bottom) with an increase in applied pressure.

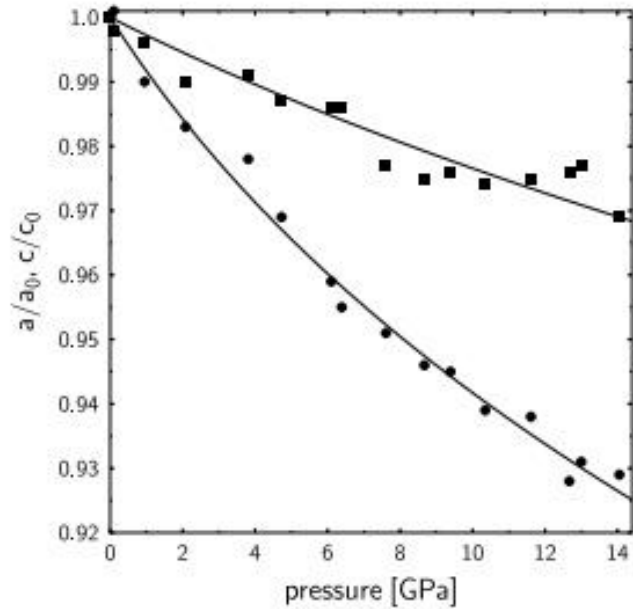


**Figure 22.** Pressure dependence of  $a/a_0$  (squares) and  $c/c_0$  (circles) for  $\text{NbS}_2$  by *Ehm et al.*

The high anisotropy ratios in the compressibility can be explained by taking an in depth Look into the structure of these materials. The **a** and **b** axes which have the lowest compression factor are made up of the layers that are connected with covalent bonded prisms. On the other hand, the covalent bonded layers are stacked on top of each other, and are held together by van-der-Waals forces parallel to the **c** axis. Hence, it can be concluded that the high compressibility along the **c** axis is driven by the fact that the van-der-Waals gaps are easily reduced by the weak nature of the attractive force, as opposed to the **a** axis, where the strong covalent bonds strongly oppose the compression and the change in interlayer distances [24].

## High Pressure Transport Measurements

Measurements of electrical resistivity as a function of temperature were taken on Te doped sample at 5 different pressure points; 0 GPa, 0.6 GPa, 1.2 GPa, 1.5 GPa, and 1.8 GPa. Data was collected at temperature range from 20 K down to 2.5 K at each pressure. The respective plot of the pressure dependence of normalized resistivity values are presented in **Fig. 23**. The superconducting transition temperature at ambient pressure for NbSe<sub>1.5</sub>Te<sub>0.5</sub> was found to be 3.35 K. The onset of T<sub>c</sub> was determined by estimating the point of interception of fitted horizontal and vertical lines.

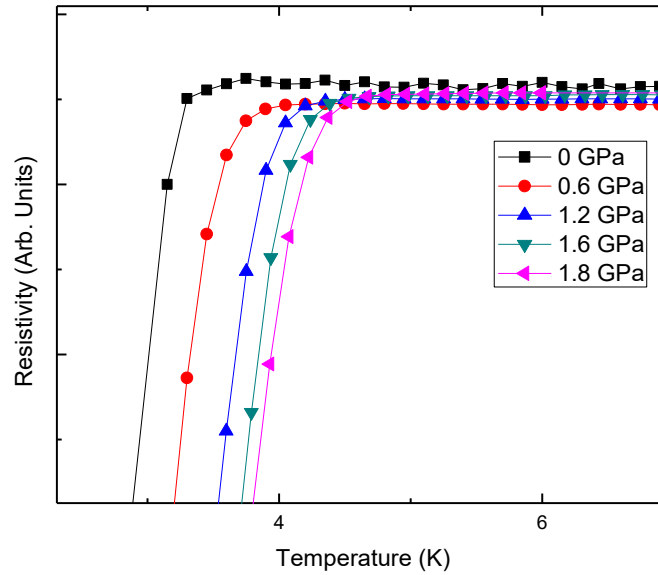


**Figure 23.** Resistivity as a function of temperature from ambient pressure up to 1.80 GPa

The ambient transition temperature for the Te-doped sample was significantly lower than the  $T_c$  of undoped NbSe<sub>2</sub>. This matches with the results obtained by *Antonova et al.* [26] for the  $T_c$  dependence of the tellurium concentration in NbSe<sub>2</sub>. From the structural point of view, the decrease in transition temperature with increasing the percentage of Te atoms is accompanied by the parameters  $a$  and  $c$  increasing. Consequently, this change can be understood by considering the fact that the distance between neighboring Nb atoms in their own plane becomes larger, and also, that there is an increase in the separation between niobium planes as well [26]. Therefore, it can be concluded that superconductivity in transition metal dichalcogenides is mainly governed by state of the atoms in Nb-Nb layers, and the correlation between the planes.

Our experimental results are, also, consistent with the work done by *Hong-Tao, et al.* where they have investigated the change in superconducting  $T_c$  for NbSe<sub>2-x</sub>Te<sub>x</sub> for Te concentrations  $x = 0, 0.1, \text{ and } 0.2$ . It was reported that the transition temperature goes down linearly by around 0.7 K for each increase of Te doping of  $x = 0.1$  [27]. This agrees fairly well with our measured ambient  $T_c$  of 3.35 K for Te concentration of  $x = 0.5$ . It was, also, observed that the temperature at which the compounds undergo CDW transition ( $T_{CDW}$ ) goes up linearly from 30.6 K to 31.9 K, explained by the fact that, since Te doping changes the lattice parameters and increases the  $c$ -axis lattice constant, the coupling between the layers could become weaker and the system could become more two-dimensional, which could account for the enhancement of the CDW instability. They have shown by transport measurements, that there are more electrons condensed into CDW state. Due to the competition of the CDW and Superconducting states, The enhancement of CDW ordering causes a decrease of density of states at Fermi surface and, thus, suppresses superconductivity.

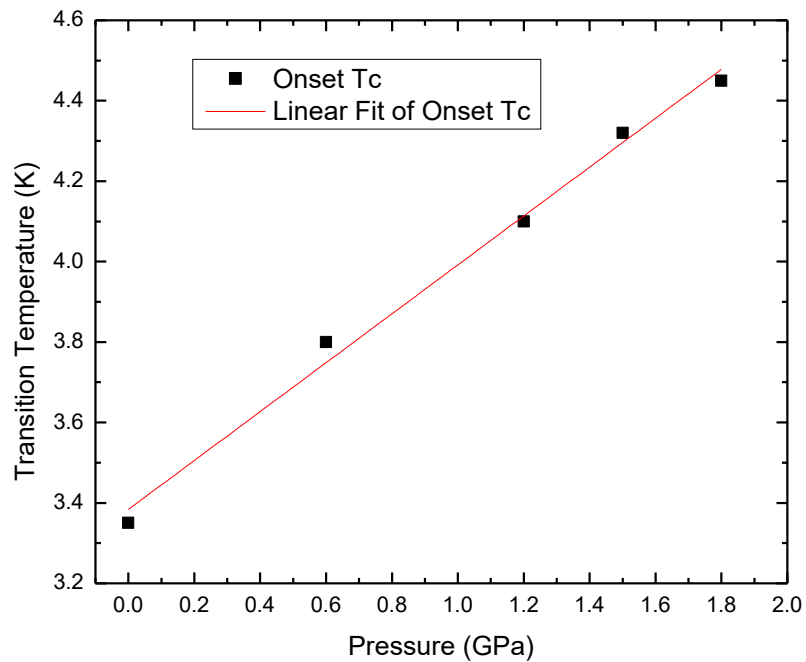


**Figure 24.** Presents the change of the superconducting temperature as a function of pressure for  $\text{NbSe}_{1.5}\text{Te}_{0.5}$

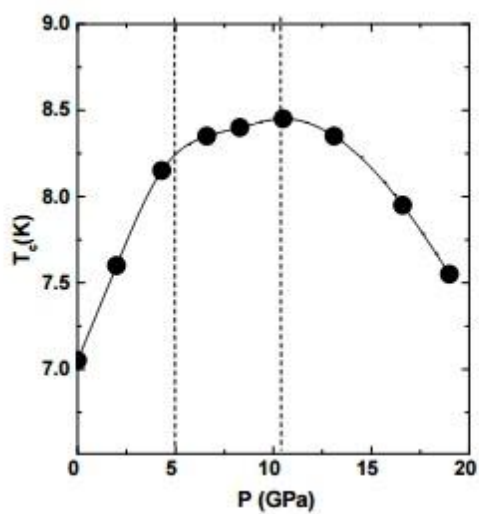


**Figure 25.** The pressure dependence of  $T_c$  for  $\text{NbSe}_2$  from *Suderow et al.*

The variation of the transition temperature  $T_c$  with application of pressure is shown in **Fig. 24**. The onset  $T_c$  goes up linearly as a function of pressure, reaching a value of 4.40 K at 1.8 GPa. This implies a rate of increase of  $T_c$  of 0.60 K/GPa. The upward trend of the change of the transition is consistent with the results found in the literature. In the paper by *Suderow et al*, **Fig. 25**, the behavior of  $T_c$  for undoped NbSe<sub>2</sub> was reported below 5 GPa, with an increase of 0.25 K/GPa. Between 5 GPa and 10.5 GPa  $T_c$  increases by a small amount of 0.05 K/GPa, followed by a decrease above 10.5 GPa of  $-0.1$  K/GPa. CDW state was found to remain present until 5 GPa, the point at which the pressure derivative of  $T_c$  starts changing slope. It was concluded that the initial increase of  $T_c$  with pressure, is mainly controlled by that of electron-phonon coupling parameter  $\lambda_1$ , whereas the pressure rate of change of parameter  $\lambda_2$  is close to zero at low pressure range. At pressures between 5 and 11 GPa  $\lambda_1$  shows a downward trend, but  $\lambda_2$  increases. Above 11 GPa, where the highest  $T_c$  is observed, both parameters show a negative slope, and  $T_c$  decreases as a consequence [28].

## Chapter 6: Conclusion

Two transition metal dichalcogenide compounds NbSe<sub>2</sub> and NbSe<sub>1.5</sub>Te<sub>0.5</sub> were successfully synthesized by a solid state preparation route. Ambient pressure x-ray diffraction confirmed a single phase with hexagonal crystal structure (space group P6<sub>3</sub>mmc) for both synthesized materials. Data analysis showed unit cell parameters  $a = b = 3.442 (2) \text{ \AA}$ , and  $c = 12.539 (2) \text{ \AA}$  for NbSe<sub>2</sub>, and  $a = b = 3.461 (2) \text{ \AA}$ ,  $c = 12.728 (5) \text{ \AA}$  for NbSe<sub>1.5</sub>Te<sub>0.5</sub>.

High pressure XRD measurements were performed to study the structural stability up to 39 GPa on both compounds. The investigation of diffraction patterns at high pressure demonstrated that the samples remained in their ambient crystal structure, without exhibiting any phase transitions up to the highest pressure studied. The change of unit cell volume as a function of pressure has been investigated. The equation of state parameters were fitted and the bulk moduli were calculated to be  $B_0 = 52 (7.4) \text{ GPa}$ , and  $61.7 (10) \text{ GPa}$  for NbSe<sub>2</sub> and NbSe<sub>1.5</sub>Te<sub>0.5</sub> respectively. The lattice compressibility analysis revealed strong anisotropy in the compression, with  $c$  axis being twice as compressible as  $a$  axis. The compression factor along  $a$  axis was estimated to be  $k_a = 0.0033 (2) \text{ GPa}^{-1}$  for NbSe<sub>2</sub>, and  $k_a = 0.0029 (3) \text{ GPa}^{-1}$  for NbSe<sub>1.5</sub>Te<sub>0.5</sub>, whereas  $k$  parallel to  $c$  axis was  $k_c = 0.0174 (3) \text{ GPa}^{-1}$  and  $k_c = 0.0115 (5) \text{ GPa}^{-1}$  for NbSe<sub>2</sub> and NbSe<sub>1.5</sub>Te<sub>0.5</sub> correspondingly. The results obtained were in good agreement with other reported values found in the literature for similar layered structure dichalcogenides.

From ambient transport measurements, the critical temperature  $T_c$  was found to be 7.1 K for NbSe<sub>2</sub> and 3.35 K for Te doped sample. We have, further, performed resistivity vs temperature measurements to investigate the  $T_c$  of NbSe<sub>1.5</sub>Te<sub>0.5</sub> as a function of hydrostatic pressures up to 1.8 GPa using the four probe resistivity technique in a piston cylinder cell. Application of pressure enhances the onset transition from 3.35 K to 4.4 K, with a pressure rate of change in transition temperature of 0.6 K/GPa.



## References

- [1]. Charles Kittel, *Introduction to solid state physics*, Seventh edition, Wiley India, 2004
- [2]. R.K.Puri, V.K.Babbar, *Solid state physics*, S.chand, 2009
- [3]. S.O.Pillai, *Solid state physics*, 6th edition, new age international publishers, 2006
- [4]. D. Dew-Hughes, *The critical current of superconductors: an historical review*, Low Temperature Physics, Vol 27, Number 9–10, 2001
- [5]. Xiaoxiang Xi, et al. *Strongly enhanced CDWs in monolayer NbSe<sub>2</sub>*. Nature nanotechnology. July, 2015
- [6]. K. H. Bennemann, et al. *History of Superconductivity: Conventional, High-Transition Temperature and Novel Superconductors*, 2008
- [7]. Miguel M. Ugeda et al. *Characterization of collective ground states in single-layer NbSe<sub>2</sub>*, Nature Physics, 2015
- [8]. H. Hosono, *J. Phys. Soc. Jpn.* **77**, Suppl. C, 1 - 8, 2008
- [9]. A. Ciechan, et al. *The Pressure Effects on Electronic Structure of Iron Chalcogenide Superconductors FeSe<sub>1-x</sub>Te<sub>x</sub>*, 2012
- [10]. Zhong-Li Liu, et al. *Novel high pressure structures and superconductivity of niobium disulfide*. January 16, 2014
- [11]. Kittel, Charles. *Introduction to Solid State Physics*. 8th edition.
- [12]. Stanford EMSI Science Teachers Workshop – July 2006
- [13]. Poirier, J.P. *Introduction to the Physics of the Earth Interior*. Second edition, 2000
- [14]. F. Birch, *J. Appl. Phys.* 9, 279, 1938
- [15]. ] <http://stwww.weizmann.ac.il/lasers/laserweb/Ch-6/C6s2t1p2.htm>
- [16]. [http://www.geo.arizona.edu/xtal//group/images/ruby\\_fluorescence.JPG](http://www.geo.arizona.edu/xtal//group/images/ruby_fluorescence.JPG)
- [17]. Mao, HK., et al. *J. Appl.Phys.* 49, 3276, 1978
- [18] S. Mishra. *Synthesis and Characterization of Superconductor Composite Bi<sub>2</sub>Sr<sub>2</sub>Ca<sub>1</sub>Cu<sub>2</sub>O<sub>8</sub>/La<sub>0.85</sub>Sr<sub>0.15</sub>MnO<sub>3</sub>*. 2012
- [19]. <http://www.geocities.ws/engineering.physics/hall2.gif>

- [20]. Van der Pauw, L. J. "A Method of Measuring Specific Resistivity and Hall Effect of Discs of Arbitrary Shape." Philips Research Reports 12.1 1958
- [21]. Materials Data Incorporated, 1224 Concannon Blvd., Livermore, California 94550, USA
- [22]. A. Meerschaut. *Crystal structure studies of the 3R-Nb<sub>1.09</sub>S<sub>2</sub> and the 2HNbSe<sub>2</sub> compounds: correlation between nonstoichiometry and stacking type.* Materials Research Bulletin 36 (2001) 1721–1727
- [23]. A. P. Hammersley, S. O. Svensson, M. Hanfland, A. N. Fitch, and D. Häusermann, High Press. Res. 14, 235 1996
- [24]. L. Ehm , K. Knorr and W. Depmeier. The high-pressure behaviour of 3R-NbS<sub>2</sub>. 10 Sep, 2012.
- [25]. Jones, R.E.; Shanks, H.R.; Finnemore, D.K.: *Pressure effect on superconducting NbSe<sub>2</sub> and NbS<sub>2</sub>.* Phys. Rev. B 6 (1972) 835-838
- [26]. E. A. ANTONOVA, et al. P. N. Lebedev Physics Institute, U.S.S.R. Academy of Sciences. Zh. Eksp. Teor. Fiz. 59, 54-58 (July, 1970)
- [27]. Wang Hong-Tao, Chinese Physics, Vol 16 No 8, August 2007 Chin. Phys. Soc.
- [28]. H. Suderow, et al. Pressure Induced Effects on the Fermi Surface of Superconducting 2H-NbSe<sub>2</sub>. PRL 95, 117006 (2005)

## Curriculum Vitae

### **Vahe Mkrtchyan**

Phone: (702)-481-2787

Email address: Mkrtchy3@unlv.nevada.edu

#### Education:

Bachelor of Science, Physics, 2014

University of Nevada, Las Vegas

#### Thesis Title:

STRUCTURAL BEHAVIOR OF  $\text{NbSe}_x\text{Te}_{2-x}$  SUPERCONDUCTORS UNDER HIGH PRESSURE

#### Thesis Committee:

Andrew Cornelius, Committee Chair

Ravhi Kumar, Committee Co-Chair

Michael Pravica, Committee Member

Thomas Hartmann, Graduate College Representative